

Revisiting Lithium- and Sodium-Ion Storage in Hard Carbon Anodes

Hoseong Kim, Jong Chan Hyun, Do-Hoon Kim, Jin Hwan Kwak, Jin Bae Lee, Joon Ha Moon, Jaewon Choi, Hee-Dae Lim, Seung Jae Yang, Hyeong Min Jin, Dong June Ahn, Kisuk Kang, Hyoung-Joon Jin,* Hyoung-Kyu Lim,* and Young Soo Yun*

The galvanostatic lithiation/sodiation voltage profiles of hard carbon anodes are simple, with a sloping drop followed by a plateau. However, a precise understanding of the corresponding redox sites and storage mechanisms is still elusive, which hinders further development in commercial applications. Here, a comprehensive comparison of the lithium- and sodium-ion storage behaviors of hard carbon is conducted, yielding the following key findings: 1) the sloping voltage section is presented by the lithium-ion intercalation in the graphitic lattices of hard carbons, whereas it mainly arises from the chemisorption of sodium ions on their inner surfaces constituting closed pores, even if the graphitic lattices are unoccupied; 2) the redox sites for the plateau capacities are the same as those for the closed pores regardless of the alkali ions; 3) the sodiation plateau capacities are mostly determined by the volume of the available closed pore, whereas the lithiation plateau capacities are primarily affected by the intercalation propensity; and 4) the intercalation preference and the plateau capacity have an inverse correlation. These findings from extensive characterizations and theoretical investigations provide a relatively clear elucidation of the electrochemical footprint of hard carbon anodes in relation to the redox mechanisms and storage sites for lithium and sodium ions, thereby providing a more rational design strategy for constructing better hard carbon anodes.

1. Introduction


Intercalation-based host materials that can store lithium ions in their crystallographic lattices have led to the commercial success of rechargeable lithium-ion batteries (LIBs).^[1,2] The robust host structures provide them with high reversibilities and cycling stabilities, enabling omnidirectional market-share expansion and beginning a new industrial era.^[1–3] Over the last decades, studies have been extensively carried out to optimize and discover advanced active materials with relatively high electrochemical performances.^[4–6] Accordingly, active cathode materials have been significantly modified from the initial LiCoO₂ system to more advanced ternary mixture systems of transition metals (e.g., Co, Ni, and Mn), resulting in a substantial increase in reversible capacities and redox potentials.^[4] By contrast, the original graphite-based intercalation compound anodes have maintained their dominance, which is mostly due to the absence of

H. Kim, H.-J. Jin
Program in Environmental and Polymer Engineering
Inha University
Incheon 22212, South Korea
E-mail: hjjin@inha.ac.kr

J. C. Hyun, D. J. Ahn, Y. S. Yun
KU-KIST Graduate School of Converging Science and Technology
Korea University
145 Anam-ro, Seongbuk-gu, Seoul 02841, South Korea
E-mail: c-syun@korea.ac.kr

D.-H. Kim, K. Kang
Department of Materials Science and Engineering Research Institute of
Advanced Materials
Seoul National University
1 Gwanak-ro, Gwanak-gu, Seoul 08826, South Korea

J. H. Kwak, H.-D. Lim
Energy Storage Research Center
Korea Institute of Science and Technology (KIST)
Seoul 02792, South Korea

 The ORCID identification number(s) for the author(s) of this article can be found under <https://doi.org/10.1002/adma.202209128>.

J. B. Lee
Korea Basic Science Institute
Daejeon 169-147, South Korea

J. H. Moon, J. Choi
Department of Chemistry
Gyeongsang National University
Jinju 52828, South Korea

S. J. Yang
Department of Chemistry and Chemical Engineering
Education and Research Center for Smart Energy and Materials
Inha University
100, Inha-ro, Michuhol-gu, Incheon 22212, South Korea

H. M. Jin
Department of Organic Materials Engineering
Chungnam National University
Daejeon 34134, South Korea

D. J. Ahn
Department of Chemical and Biological Engineering
College of Engineering
Korea University
145, Anam-ro, Seongbuk-gu, Seoul 02841, South Korea

DOI: 10.1002/adma.202209128

competitive anode materials with feasible chemistry and mass scalability.^[1] Although alternative anodes, such as high-capacity silicon, have brought about significant attention for the next-generation chemistry, their large volume expansion and unanticipated side reactions induced by the interfacial instability make their widespread adoption in commercial rechargeable batteries a daunting task.^[7,8]

Hard carbon is a disordered graphitic carbon material with irregular polycrystalline microstructures bearing numerous topological defects, prismatic surfaces, and closed pores.^[9] Owing to its complex nature, it generally exhibits highly complicated lithium-ion storage behaviors, distinct from the simple intercalation reaction in graphite.^[10,11] Accordingly, its lithiation mechanisms and the corresponding redox sites have been relatively poorly understood despite its industrial importance. The undetermined lithium-ion storage properties hinder the advancement of hard carbon anodes in electrochemical performance, causing them to fall behind graphite in the LIB market. On the other hand, hard carbon anodes in sodium-ion batteries (SIBs) have been widely studied because of their higher sodium-ion storage capacities than that of graphite-like materials.^[12–21] Sodium ions can be inserted inside the structure of hard carbons through various redox mechanisms, which are presented by their galvanostatic sodiation/desodiation profiles.^[11–21] Prior studies have focused on identifying the respective sodiation mechanisms in distinctive voltage regions in the form of a sloping or plateau section.^[12–18] Nonetheless, the specific redox sites are the subject of intense debate. Moreover, the large variations in the reversible capacities of hard carbon materials from different synthetic routes confound our efforts to elucidate the sodium-ion storage mechanism in hard carbon anodes and their intrinsic redox potentials.

Herein, a systematic investigation is conducted on the redox mechanisms of various hard carbons bearing distinct local microstructures with respect to the lithium- and sodium-ion storage sites and their corresponding lithiation and sodiation voltage profiles. The extensive analysis of material properties, electrochemical characterizations using galvanostatic methods, and sequential electrochemical tests using both lithium- and sodium-ion charge carriers are performed on microstructure-tuned hard carbon series samples. Further, first-principle calculations are employed to clarify the complex experimental results

and their interrelationships. The results of this comprehensive study demonstrate the high potential of hard carbon anodes for use in SIBs and LIBs and provide guidelines for constructing better hard carbon anodes.

2. Results and Discussion

Hard carbons with different graphitic microstructures were prepared via the thermal annealing of commercial hard carbon at temperatures of 1200, 1600, 2000, 2400, and 2800 °C, designated as HC1200, HC1600, HC2000, HC2400, and HC2800, respectively. As the annealing temperatures were increased, the primary graphitic structures of the hard carbon samples developed into relatively dense structures composed of relatively large graphenic domain sizes (L_a , 1.6–4.6 nm) and relatively thick graphitic layers (L_c , 1.2–29.8 nm).^[22–25] Additionally, the secondary microstructures comprising primary graphitic domains contained numerous closed pores with a relatively high annealing temperature, whose radii gradually increased ranging from 0.96 to 2.49 and 0.83 to 2.75 nm in small-angle X-ray scattering (SAXS) and small-angle neutron scattering analyses, respectively.^[26,27] Despite the transitions in the primary and secondary microstructures, their contour morphologies minimally changed during annealing up to 2800 °C (Texts S1–S3, Figures S1–S11, and Tables S1–S4, Supporting Information). Schematic diagrams (Figure 1a) depict the microstructural evolution of the graphitic structures for each hard carbon prepared at different annealing temperatures.

In the following text, we first clarify the terminologies for the redox reaction mechanisms in hard carbon (Figure S12, Supporting Information), which are often ambiguously used in previous studies.^[10–21] Surface chemisorption is defined as the direct reduction of alkali ions on an electrochemically active surface, including open pores near the outermost part of the particles. “Bulk insertion” refers to the process of storing alkali ions within bulk particles, which can be categorized into three distinct storage mechanisms: 1) “bulk chemisorption” on the defective surface of the inner graphitic domains, 2) “intercalation” in the graphitic interlayers, and 3) “nanoclustering” in the inner closed pore volume. The three insertion mechanisms depend on the interlayer distance and the presence of defect sites in the primary graphitic domains within the secondary microstructure containing closed pores, for which the quantitative criteria will be discussed later.

The electrochemical lithium-ion and sodium-ion storage behaviors of a series of hard carbon samples were characterized at both 25 and 60 °C. In the room-temperature galvanostatic discharge/charge (RT-GDC) in lithium cells (Figure 1b), all samples exhibited sloping voltage profiles between 1.2 and 0.01 V vs Li⁺/Li. The capacity gradually decreased as the annealing temperature increased from 1200 to 2400 °C, whereas it marginally increased at 2800 °C. Notably, the HC1200 and HC1600 electrodes displayed low-voltage plateau capacities at ≈0 V. As voltage overshooting induced by lithium-metal nucleation reactions typically occurs at lower voltages than the applied cutoff voltage of –0.01 V, the plateau capacities are distinct from lithium-metal plating capacities (inset of Figure 1b).^[28] The high-temperature galvanostatic discharge/charge (HT-GDC) at

K. Kang
School of Chemical and Bioengineering Institute of Engineering
Research College of Engineering
Seoul National University
1 Gwanak-ro, Gwanak-gu, Seoul 08826, South Korea

H.-J. Jin
Department of Polymer Science and Engineering
Inha University
Incheon 22212, South Korea

H.-K. Lim
Division of Chemical Engineering and Bioengineering
Kangwon National University
Chuncheon, Gangwon-do 24341, South Korea
E-mail: hklim@kangwon.ac.kr

Y. S. Yun
Department of Integrative Energy Engineering
Korea University
145, Anam-ro, Seongbuk-gu, Seoul 02841, South Korea

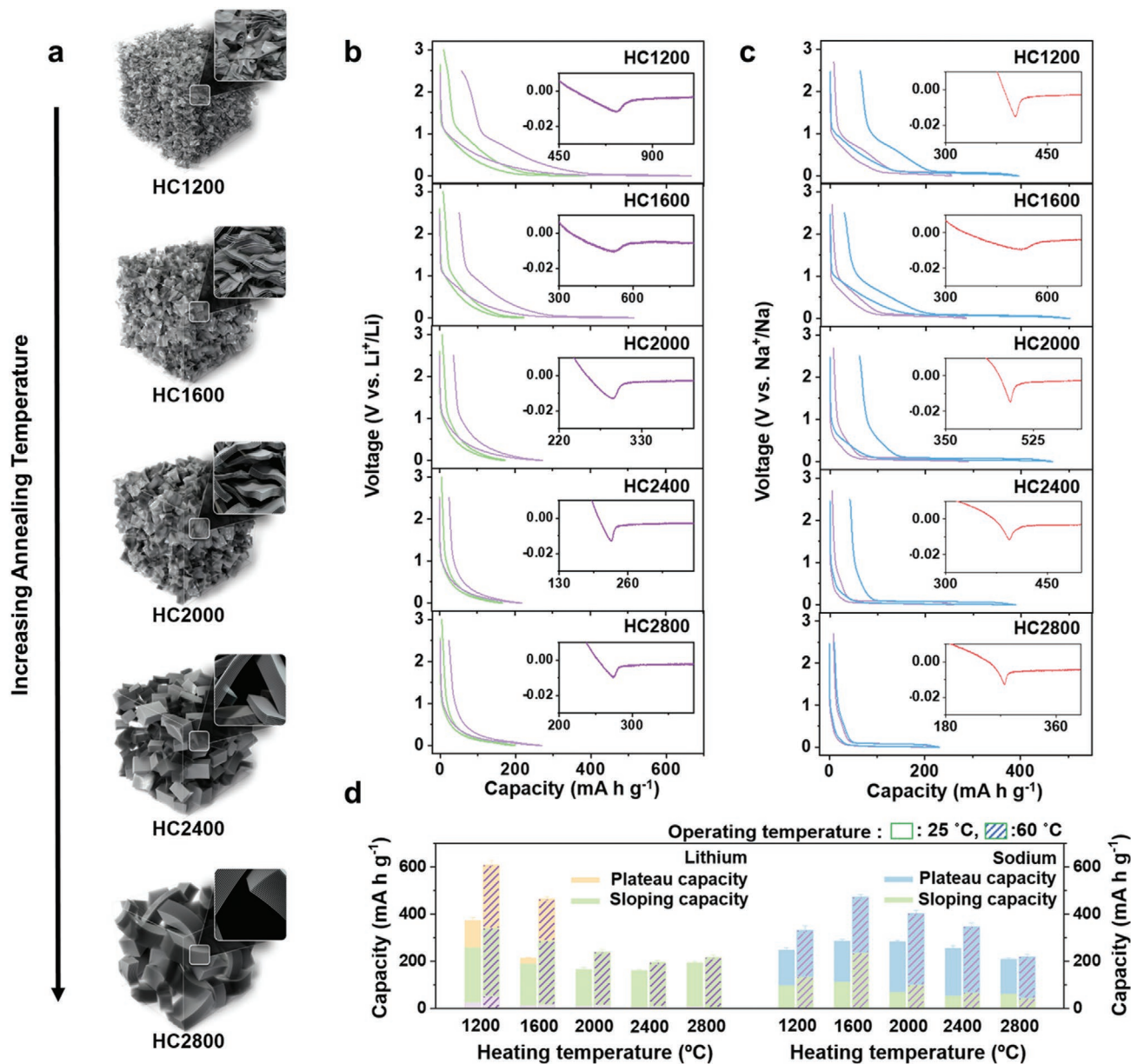


Figure 1. Microstructural transition of hard carbon series samples with annealing temperatures and their lithium- and sodium-ion storage behaviors. a) Schematic images for the different microstructures; b) galvanostatic lithiation and delithiation profiles over a voltage window of -0.01 to 3.0 V vs Li^+/Li at a current density of 20 mA g^{-1} at 25 (green) and 60 °C (purple); c) galvanostatic sodiation and desodiation profiles over a voltage window of -0.01 to 2.7 V vs Na^+/Na at a current density of 20 mA g^{-1} at 25 (blue) and 60 °C (pink); and d) capacity bar graphs for the lithium/sodium sloping and plateau capacities at the different operating temperatures of 25 and 60 °C.

60 °C exhibited overall relatively high reversible capacities, with the plateau capacities of HC1200 and HC1600 being significantly high, whereas HC2000, HC2400, and HC2800 continue to lack plateau capacities (Figure 1b). This result suggests that the lack of plateau capacities in HC2000, HC2400, and HC2800 was likely due to the intrinsic redox inactiveness at the voltage rather than kinetic factors.

In contrast to the lithium-ion storage behavior, all RT-GDC and HT-GDC profiles in the sodium cells exhibited long-range plateau capacities at a similar voltage of ≈ 0 V vs Na^+/Na (Figure 1c). The low-voltage plateaus occurred at the same

voltage for all the samples, regardless of the distinct graphitic microstructures with varying annealing temperatures, as indicated by the dV/dQ curves (Figure S13, Supporting Information). Considering the significant difference in the primary graphitic structures among the samples, it may be inferred that the low-voltage plateau was not likely due to the intercalation of sodium ions into the graphitic region. Compared with the electrochemical activities in the lithium cells, the RT-GDC and HT-GDC profiles in the sodium cells exhibited sloping capacities in the same voltage range as those in lithium cells; however, they were consistently smaller than the

corresponding lithium-ion sloping capacities. Moreover, the maximum sodium-ion plateau capacity was observed with the HC2000 electrode, whereas it displayed a nearly negligible plateau capacity in the lithium cells. These experimental findings strongly suggest that the sodium-ion storage behavior in hard carbons fundamentally differs from the lithium-ion storage behavior, particularly for samples prepared at relatively high annealing temperatures of ≥ 2000 °C.

The reversible lithium-ion storage capacities of HC2000, HC2400, and HC2800 were in the range 166–195 and 218–241 mA h g⁻¹ in the RT-GDC and HT-GDC profiles, respectively, and were primarily induced by the sloping voltage region (Figure 1d). In the RT-GDC/HT-GDC profiles of the lithium cells, HC1200 and HC1600 had greater sloping capacities of 233/287 and 177/271 mA h g⁻¹, respectively. Despite this, the presence of plateau capacities corresponding to 268 and 176 mA h g⁻¹ nearly doubled their overall reversible capacities relative to those of the other samples. By contrast, all the samples in the sodium cells exhibited long-range sodiation plateau capacities corresponding to 176–303 mA h g⁻¹. Further, the maximum plateau capacity exceeded the overall lithium-ion storage capacities of the high-temperature annealed samples, such as HC2000, HC2400, and HC2800, as well as the highest reversible lithium-ion sloping capacity (≈ 287 mA h g⁻¹) for HC1200 in the HT-GDC profiles. These findings raise questions regarding the precise lithium- and sodium-ion storage mechanisms at the sloping and plateau voltage sections.

To clarify the lithium- and sodium-ion storage sites in hard carbon, a sequential electrochemical analysis employing sodium-ion and lithium-ion charge carriers was conducted for the HC1200 anode, which has long-range low-voltage plateau capacities in both lithium and sodium systems (Figure 2). Figure 2a demonstrates that in the first sodiation process with a cutoff voltage of -0.01 V vs Na⁺/Na (0.32 V vs Li⁺/Li), the signature sodium-ion storage profile has both sloping (step I) and plateau (step II) capacities of ≈ 275 mA h g⁻¹. We reassembled the lithium half-cell after removing the fully sodiated anode from the sodium half-cell, in preparation for the lithiation procedure. Notably, in the subsequent lithiation procedure (step III), an additional sloping capacity of ≈ 250 mA h g⁻¹ was delivered. The sloping capacity observed in the narrow voltage window between 0.32 and -0.01 V vs Li⁺/Li was comparable to that observed in the original lithiation profile (Figures 1b and 2a). Additionally, $\approx 70\%$ of the lithiated capacity was reversibly extracted from the narrow operating voltage window (step IV), which was followed by a plateau (step V) and sloping capacity (step VI) regions corresponding to steps II and I in the delithiation/desodiation process. These findings suggest that a significant portion of the active sites for the lithium sloping capacity was nearly empty even after the initial full sodiation process. Additionally, the in situ electrochemical impedance spectroscopy (EIS) profiles for steps I and III exhibited charge-transfer resistance (R_{ct}) values that were comparable to their intrinsic R_{ct} values observed in the respective sodium and lithium half-cell tests (Figures S14–S16, Supporting Information). This indicated that the lithiation process was not impeded by the sodium ions filling the inside of the hard carbon. Moreover, the same experiments employing the HC2000 and HC2800 anodes reproduced similar results, confirming that lithium and sodium ions had different redox

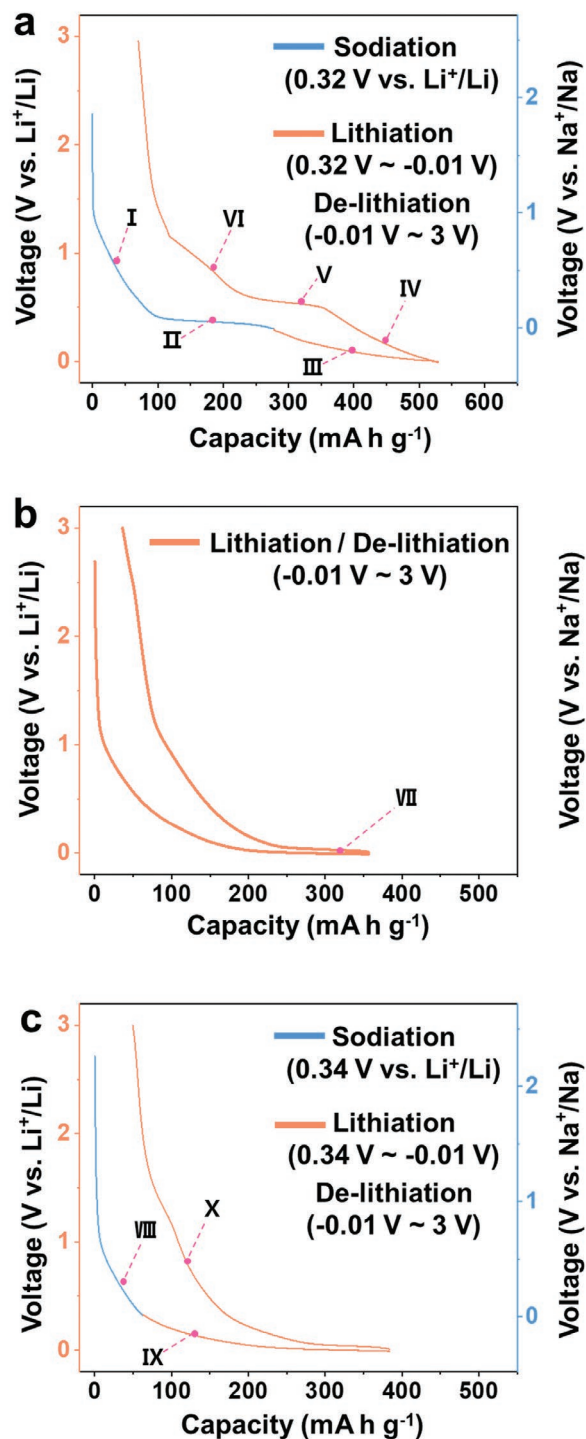


Figure 2. Sequential electrochemical tests using both lithium- and sodium-ion charge carriers for the hard carbon anode, HC1200. a) Galvanostatic profiles for the first sodiation by -0.01 V vs Na⁺/Na, followed by lithiation/delithiation in the operating voltage window between 0.32 and -0.01 V for lithiation and between -0.01 and 3 V for delithiation vs Li⁺/Li at a current density of 20 mA g⁻¹; b) galvanostatic lithiation/delithiation profiles in the operating voltage window of -0.01 to 3.0 V vs Li⁺/Li at a current density of 20 mA g⁻¹; and c) galvanostatic profiles for the first sodiation by 0.01 V vs Na⁺/Na, followed by lithiation/delithiation in the operating voltage window between 0.30 and -0.01 V for lithiation and between -0.01 and 3 V for delithiation vs Li⁺/Li at a current density of 20 mA g⁻¹.

sites in the sloping voltage section (Figure S17, Supporting Information).

As shown in Figure 2b, lithiation/delithiation tests were subsequently carried out for the HC1200 cell that was used for the sequential test. In this subsequent full lithiation process, the original lithium storage capacity was recovered, including the plateau capacity at ≈ 0 V (step VII), which was absent in the fully sodiated state (step III, Figure 2a). This result for the second consecutive cycle indicated that the active sites for the lithium- and sodium-plateau capacities were likely to overlap, thereby becoming available for the lithiation only after the desodiation. This speculation was verified by a series of sodiation and lithiation experiments. As shown in Figure 2c, the HC1200 anode was retrieved from the lithium cell after the experiment shown in Figure 2b and alternatively reassembled in sodium and lithium half-cells. Initially, the HC1200 anode was sodiated down to ≈ 0.01 V vs Na^+/Na , which showed a characteristic sloping discharge capacity (step VIII). Further, it was disassembled again and reassembled in a lithium cell for the complete lithiation (step IX). In this additional lithiation process of step IX, we observed sloping and plateau capacities that were nearly identical to the initial lithiation profile shown in Figure 1b, which were reversibly delithiated/desodiated from the HC1200 anode (step X). This series of cyclic experiments demonstrated that the sodiation process filled by the sloping voltage section did not impede the subsequent lithiation behavior, suggesting that the major storage sites of the sodium and lithium sloping voltage capacities were distinct from one another. However, their plateau capacities were attributed to the ion storage at the same sites. Ex situ field-emission transmission microscopy (FE-TEM) images characterized after full lithiation and sodiation in HC1200 reveal the presence of lithium and sodium metal nanoclusters, supporting that the closed pores are the same storage sites for the lithium and sodium plateau capacities (Figure S18, Supporting Information).

We attempted to elucidate the experimental lithium/sodium-ion storage behaviors from first-principle calculations. Various types of perfect and imperfect basal or edge sites were considered for the lithiation/sodiation, and the potentials were calculated for surface chemisorption (Figure 3a,b and Figure S19 (Supporting Information)). The perfect graphitic basal plane and fully hydrogenated zigzag/armchair edge sites had large negative reduction voltages, preventing surface chemisorption within the experimental voltage range. By contrast, several structural defects increased the lithium/sodium-ion affinity, enabling them to function as viable redox sites for both ions in the sloping voltage ranges. This was because the increased electron affinity of the defective sites induced a strong electrostatic interaction between the surface and ions.^[29] Additionally, the relative surface-chemisorption voltage ranges of the lithium/sodium ions were comparable, indicating that their surface-chemisorption behaviors were inherently similar.

The surface-chemisorbed lithium/sodium ions could diffuse into the inner region of the hard carbon particles owing to the local potential and concentration gradient (bulk insertion). In the complex internal secondary microstructure composed of the disordered arrangement of the primary graphitic domains with different sizes, defects, and interlayer distances, depending on the annealing temperature, the inserted ions could be either

chemisorbed on the inner closed pore surfaces (bulk chemisorption) or inserted inside the graphitic domains (intercalation). The bulk chemisorption was analogous to the surface chemisorption, in that the inserted ion mainly interacted with the surface in an internal pore larger than the critical size. By contrast, the intercalation process can be defined such that the inserted ion is stored by interaction with bilateral surfaces, either in a graphitic lattice domain or in a very small closed pore with a diameter smaller than the critical diameter. To quantitatively determine the criteria of the critical interlayer distance for bulk chemisorption and intercalation, the stabilization trends of each ion were calculated in the various stacking combination models with an interlayer distance range of 3.6–20 Å for the surface chemisorption (Figure 3c,d). When the interlayer distance was as large as 20 Å, the obtained voltage values were comparable to those of the surface chemisorption, and the majority of defects and surrounding sites could serve as redox sites within 0.75 V vs M^+/M . Conversely, the perfect graphite structure did not serve the same. With decreasing interlayer distance, the interaction between the ions and opposing surfaces gradually increased, and the maximum voltage value was determined to be ≈ 4 Å for lithium and 5 Å for sodium. Based on these theoretical considerations, bulk-chemisorption sites are regions with relatively large interlayer distances ($\gtrsim 6.0$ Å for lithium and > 8.0 Å for sodium) that exhibit similar redox potentials to surface chemisorption. Further, the increased voltage ranges with the interlayer distances of 3.6–6.0 Å for lithium and 4.0–8.0 Å for sodium were categorized as the intercalation region.

Notably, a significant difference in the lithium/sodium-ion storage behaviors occurred in the graphitic interlayer distances at ≈ 3.6 –4.0 Å. In the graphitic lattice domains (d -spacings of ≤ 3.78 Å) of the hard carbon samples, the sloping voltage region was dominated by the lithium-ion intercalation process. By contrast, the same interlayer distances were too small for sodium-ion intercalation; consequently, bulk chemisorption predominantly occurred during the sodiation process, even if the graphitic lattices were unoccupied. Partial sodium-ion intercalation could occur owing to the large d -spacing variation, particularly in samples with low annealing temperatures. However, the intercalated phase was present only in the near-edge region and could not propagate into the inner lattice region owing to the intrinsically high diffusion barrier of the sodium ions (Figure S20, Supporting Information). Consequently, the sodium-ion intercalation capacities of all the samples from the hard carbon series were relatively low in the sloping-capacity section. This theoretical interpretation explains several experimental results in the sloping voltage section, including the significant decrease in sodiation sloping capacities with increasing annealing temperature, the overall increase in lithiation capacities, particularly on HC2800, and the occurrence of undisturbed lithium-ion sloping capacities in the fully sodiated states. The antithetic lithium-ion and sodium-ion storage behaviors were confirmed through ex situ optical image observation for fully lithiated and sodiated hard carbon series (Figure S21, Supporting Information). Stage I intercalation compounds are known to have a golden color, whereas the stage II, III, and IV intercalation compounds exhibit a blue color.^[30–32] The fully lithiated hard carbon electrodes reveal that the black-colored

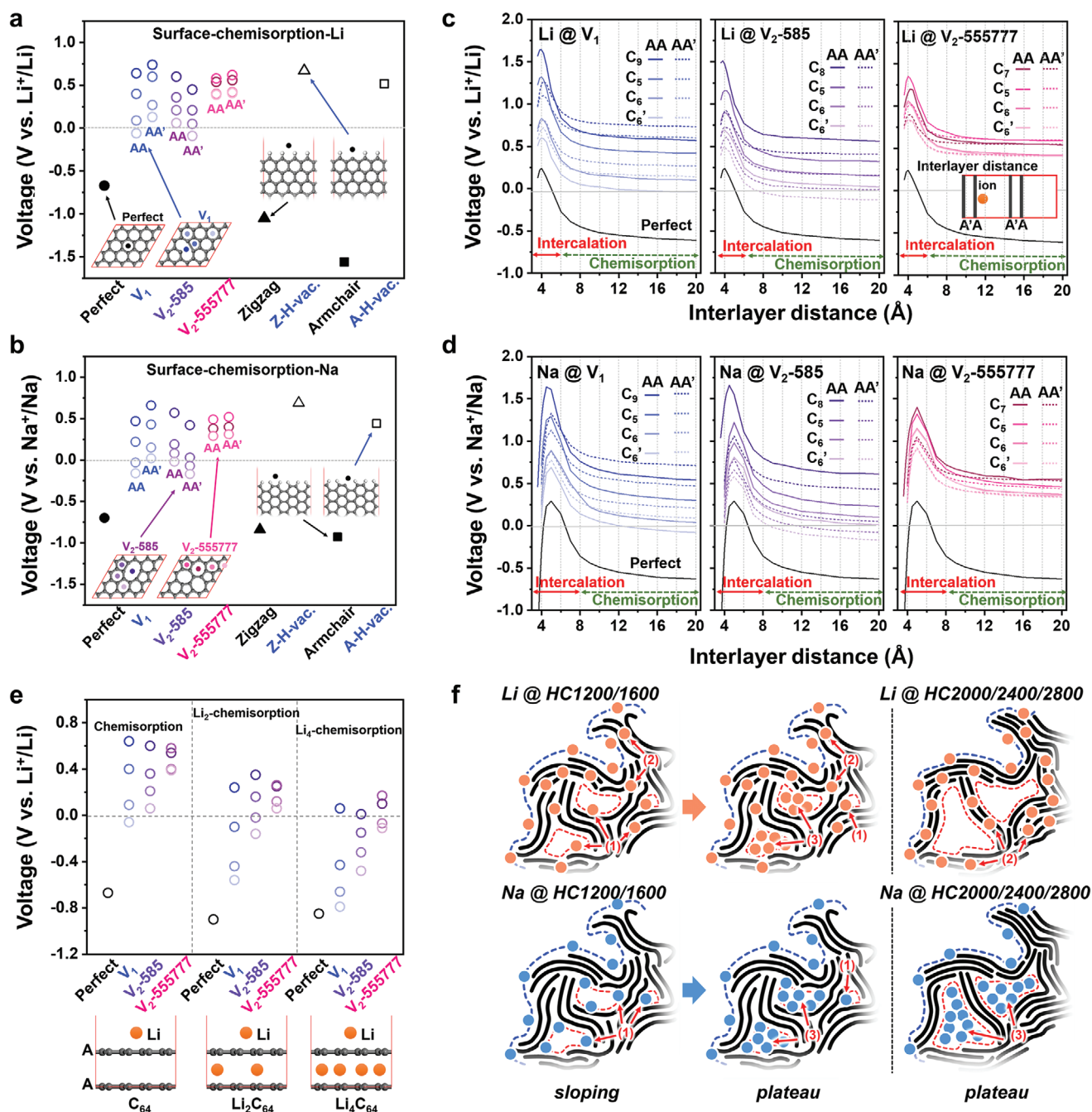


Figure 3. First-principle calculations and schematic illustrations for the lithium/sodium-ion storage behaviors of the hard carbon series samples with different microstructures. a,b) Calculated surface-chemisorption voltages of lithium and sodium ions on different types of defective sites on basal and edge structures; defective structures included carbon monovacancy (V₁) and divacancy (V₂₋₅₈₅ and V₂₋₅₅₅₇₇₇) on graphene basal planes, as well as hydrogen monovacancies on zigzag (Z-H-vac.) and armchair (A-H-vac.) graphene edges; c,d) stabilization trends of lithium and sodium ions within various stacking combinations of defective graphene basal planes over the interlayer distance range of 3.6–20 Å; e) changes in the surface-chemisorption voltage of lithium ion, depending on the sublayer intercalation ratio; f) schematics of the lithium and sodium storage mechanism based on the microstructural changes of the hard carbons by thermal annealing: 1) bulk chemisorption, 2) intercalation, and 3) nanoclustering.

pristine electrode transforms into dark blue colors for HC1200, HC1600, HC2000, and HC2400, and dark yellow color for HC2800 (Figure S21a–e, Supporting Information). The color change indicates that lithium-ion intercalation reaction happens in all the samples, where lithium intercalation compounds

of stage II, III, and IV were formed for HC1200, HC1600, HC2000, and HC2400, whereas a stage I intercalation compound is mainly formed for HC2800. By contrast, all the sodiated hard carbon samples show no color change (Figure S21f–j, Supporting Information). The pristine black color was

maintained after full sodiation. The unfavorable sodium-ion intercalation behavior was also confirmed by in situ X-ray diffraction (XRD) data of HC1200 obtained during sodiation/desodiation cycling (Figure S22, Supporting Information). In the in situ XRD data, the graphite (002) peak shift was not observed, and almost same peak intensities were found in the same 2θ region during sodiation/desodiation process, supporting the ex situ observation and first-principle calculation results.

Figure 3e shows the variations in the chemisorption potential based on the number of lithium ions intercalated in the sublayer of the AA graphitic surfaces. As the concentration of intercalated lithium ions increased, all chemisorption potentials gradually decreased, resulting in a significant decrease in the number of accessible chemisorption sites. Thus, the relationship between the bulk chemisorption and intercalation capacities is a crucial indicator for determining whether or not hard carbon samples exhibit low-voltage plateau capacities. Numerous bulk-chemisorbed ions filled a few nanometer-scale closed pores surrounded by graphitic domains, and at ≈ 0 V, the weakly chemisorbed ions were released from the defective surface, resulting in a two-phase nanoclustering process in the ion-saturated inner surfaces of the closed pores. Therefore, long-range sodiation plateau capacities were achieved in all the samples because of their poor intercalation properties, which did not impede the bulk chemisorption of the sodium ions (Figure 3f). By contrast, the relative ratio of the inner pores surrounded by the surfaces of the lithium-intercalated graphitic lattice domains was significantly increased, particularly in samples subjected to high-temperature annealing, which inhibited the lithium-ion chemisorption and the subsequent nanoclustering process. Consequently, only HC1200 and HC1600, which contained significantly more defective graphitic structures, exhibited low-voltage plateau capacities (Figure 3f).

The nanoclustering reaction should be spatially constrained by the closed pore volume, leading to a pore-volume-dependent variation in the plateau capacity. To confirm the quantitative capacity–pore relationship, the sodium volume fraction (Φ_{Na}) filled by the sodium nanoclustering and the closed pore volume (Φ_{pore}) obtained from the model fitting of the SAXS data were compared for the respective hard carbon samples (Text S2, Figure S8, and Table S5, Supporting Information). From the plateau capacity in the fully sodiated hard carbons, the Φ_{Na} was calculated using Equation (1)

$$\frac{C_{\text{Na}} \times D_{\text{Na}}}{C_{\text{v,Na}}} = \Phi_{\text{Na}} \quad (1)$$

where C_{Na} , D_{Na} , and $C_{\text{v,Na}}$ are the experimentally obtained sodium plateau capacity, theoretical sodium density, and theoretical volumetric capacity of sodium, respectively. As shown in Figure 4a, the overall Φ_{Na} variation trend was similar to that of the Φ_{pore} values, confirming a correlation between the plateau capacity and pore volume. Further, the relatively large gap between the Φ_{Na} and Φ_{pore} values on HC2800 revealed that the dense graphitic structure could kinetically obstruct the nanoclustering reaction; therefore, proper graphitic local ordering could provide significantly high sodium plateau capacities. To further clarify the trend, bulk densities (D_{HC} and $D_{\text{HC-SAXS}}$, respectively) of the samples were calculated using the Φ_{Na} and

Φ_{pore} values, and the calculated bulk densities were compared with experimentally obtained bulk densities ($D_{\text{HC-column}}$) in a density gradient column filled with benzene and 1,1,2,2-tetrabromoethane (Table S5, Supporting Information). The D_{HC} values were obtained by multiplying the calculated carbon volume fractions (Φ_{C} : $1 - \Phi_{\text{Na}}$) and the hard carbon structure densities ($D_{\text{HC,struct.}}$) using Equation (2)

$$D_{\text{HC,struct.}} = D_{\text{graphite}} \times d_{002,\text{graphite}} / d_{002,\text{hard-carbon}} \quad (2)$$

where D_{graphite} , $d_{002,\text{graphite}}$, and $d_{002,\text{hard-carbon}}$ are the bulk density (2.26 g cm^{-3}) of graphite, d -spacing (0.334 nm) of graphite, and d -spacing of the hard carbon sample, respectively. Additionally, the $D_{\text{HC-SAXS}}$ values were obtained by multiplying the experimental carbon volume fractions (Φ_{C} : $1 - \Phi_{\text{pore}}$) and the $D_{\text{HC,struct.}}$ values, and the $D_{\text{HC-column}}$ values were obtained in the density gradient column. The overall variation trends of the bulk densities (D_{HC} , $D_{\text{HC-SAXS}}$, and $D_{\text{HC-column}}$) obtained from the three different methods coincided, supporting our claim that the sodium plateau capacities were affected by the closed pore volume (Figure 4b). Notably, the D_{HC} and $D_{\text{HC-SAXS}}$ values of the hard carbons prepared at relatively high annealing temperatures showed relatively large gaps with their $D_{\text{HC-column}}$ values, indicating that the closed pores unavailable for the sodium nanoclustering increased with the annealing temperature. The disorder parameter (f_a) derived from the model fitting of the scattering from micropores (I_{pores}) with the Teubner–Strey model in the SAXS curves explained the geometric transition of the pore structures and the corresponding reduction of the feasible sodium plateau capacities (Text S2 and Tables S3 and S4, Supporting Information).^[26,27] The f_a was related to the shape and order of the closed pores. The f_a values of HC1200 and HC1600 were ≈ 1 , which corresponded to a random two-phase mixture. This structure facilitated sodium-ion diffusion throughout the internal areas of the hard carbon particles. However, with increasing annealing temperature, the f_a values gradually approached ≈ 0.4 , indicating randomly spread globular pores. Accordingly, the partially isolated spherical pores disrupted sodium-ion diffusion into the overall closed pores, leading to limited plateau capacities.

The validity of the lithium- and sodium-ion storage mechanisms on hard carbon was demonstrated by the observed lithiation/sodiation properties of a variety of polymeric hard carbon samples (Figure 4c,d and Figures S23 and S24 (Supporting Information)). Similar to the observations in this study, the various polymeric hard carbons prepared only at the relatively low annealing temperature of ≤ 1600 °C showed the lithium plateau capacities, which were significantly lower than those of the theoretically expected plateau capacities (Figure 4c). This result revealed the considerable potential of hard carbon materials as anodes for LIBs, where the control of the lithium intercalation propensity could be a key to realizing the latent plateau capacities. Additionally, the overall polymeric hard carbons revealed the sodium plateau capacities, coinciding with our observation results for the series of hard carbon samples (Figure 4d). Notably, a significantly high plateau capacity of $\approx 355 \text{ mA h g}^{-1}$ was achieved with a sloping capacity of $\approx 165 \text{ mA h g}^{-1}$ for the polyester-derived hard carbon prepared at 2000 °C, where the highest sodium plateau capacity was almost similar to the

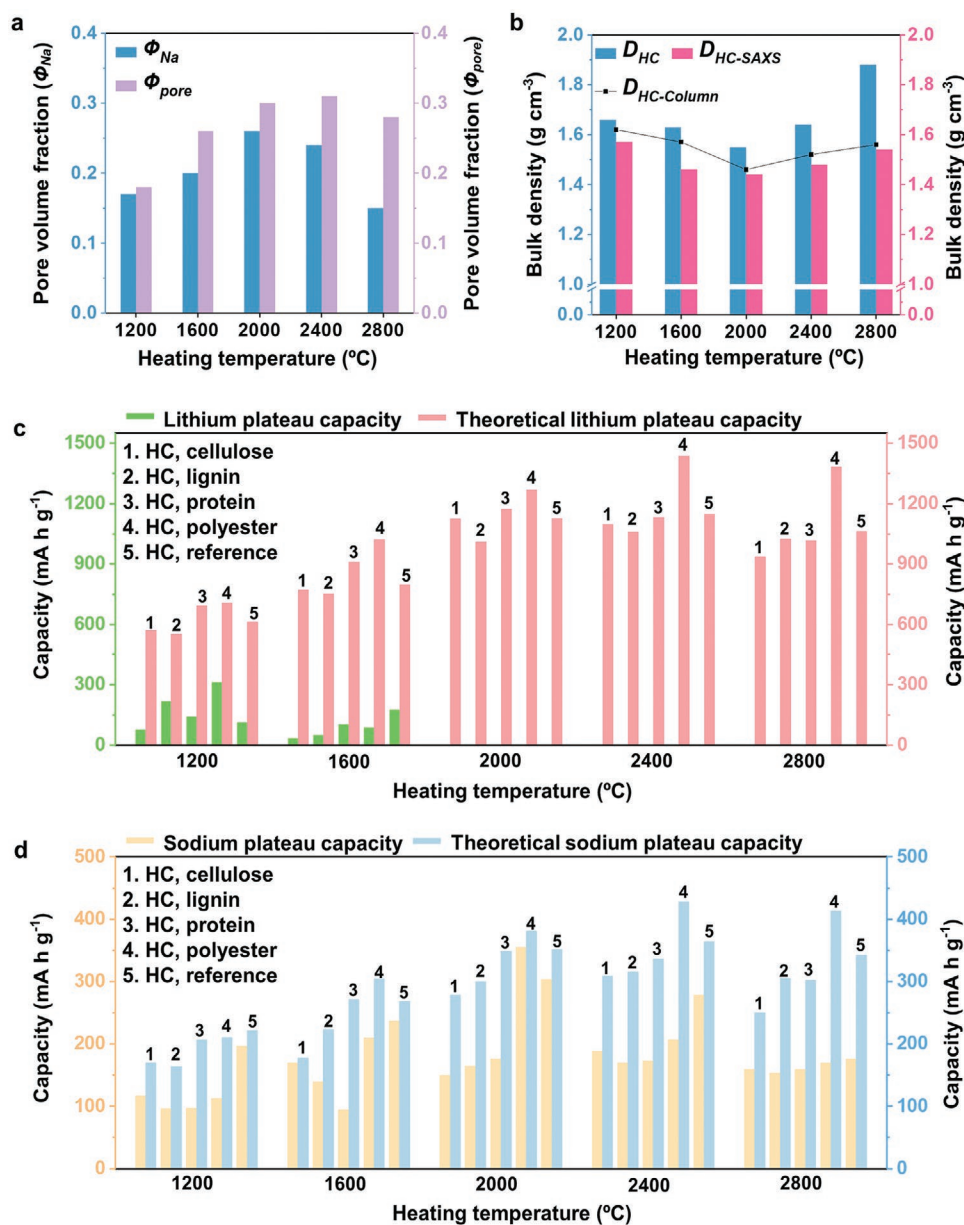


Figure 4. Comparison of the diverse bar graphs showing the close relationship between the plateau capacity and closed pore volume of hard carbon. a) Comparison of the closed pore volume fractions calculated from the low-voltage plateau capacities and the model fitting of the SAXS data. b) Comparison of the bulk densities obtained from the plateau capacity, SAXS data, and experimental characterizations. c) Comparison of the lithium plateau capacities and theoretical lithium plateau capacities obtained from the galvanostatic lithiation/delithiation profiles and experimental bulk densities, respectively. d) Comparison of the sodiation plateau capacities and theoretical sodium plateau capacities obtained from the galvanostatic sodiation/desodiation profiles and experimental bulk densities, respectively.

theoretical value. This result indicated that high-performance hard carbon anodes could be realized in SIBs by increasing the volume of the available closed pore through precise material design.

3. Conclusion

A comprehensive comparative study elucidated the lithium/sodium-ion storage sites and mechanisms of hard carbon

anodes for both sloping and plateau voltage sections and confirmed two important correlations between: i) the bulk chemisorption and intercalation capacities and ii) the closed pore volume and plateau capacities. These findings suggest that improved hard carbon anodes can be manufactured by designing optimal primary and secondary graphitic microstructures with well-developed bulk-chemisorption sites, poor intercalation characteristics, and an increased available closed pore volume. Thus, it is recommended that correlation (i) be used to increase the bulk-chemisorption sites and

decrease the intercalation capacities to construct enhanced hard-carbon anodes in LIBs. Moreover, according to the results obtained from correlation (ii), increasing the available closed pore volume can be an effective research direction for high-performance hard-carbon anodes in SIBs.

4. Experimental Section

Preparation of the Hard Carbon Series Samples: Commercial hard carbon (Carbotron S(F), Kureha Co., Japan) was heated in a graphite furnace under Ar flow from room temperature to 1200, 1600, 2000, 2400, and 2800 °C. Different heating rates of 5, 3, and 2 °C min⁻¹ were applied for the temperature ranges between room temperature to 1600 °C, 1600–2400 °C, and 2400–2800 °C, respectively. The heating temperature was hold at the target temperature for 2 h, and then, the graphite furnace was naturally cooled. The resulting hard carbon series samples were washed with ethanol several times and stored in a vacuum oven at 30 °C.

Characterization: Morphologies and local microstructures of the hard carbon series samples were characterized by field-emission scanning electron microscopy (S-4300SE, Hitachi, Japan) and FE-TEM (JEM2100F, JEOL, Japan). Crystallographic structures of the hard carbons were analyzed by XRD (Rigaku, DMAX 2500) patterns and Raman spectra (LabRAM HR Evolution, HORIBA) with a laser wavelength of 514.5 nm. For XRD analysis, a Cu K α radiation generator ($\lambda = 0.154$ nm) was used in a 2θ range of 5°–60° at 100 mA and 40 kV. From the XRD patterns, the thickness of the crystallites along the c -axis (L_c) was calculated using the Scherrer formula, $L_c = K\lambda/\beta\cos\theta$, where K , λ , β , and θ are the shape factor (commonly 0.9), the X-ray source wavelength of Cu K α (1.54 Å), the full width at half maximum in radians, and the diffracted angle, respectively. The L_a was calculated from the intensity ratio of D to G bands, I_D/I_G in Raman spectra. When $L_a > 2$ nm, Tuinstra and Koenig equation, $I_D/I_G = (\lambda)/L_a$, could be used, where $C(\lambda)$ was 4.4 on the 514 nm laser wavelength. In case of $L_a < 2$ nm, Ferrari and Robertson relationship, $I_D/I_G = C'(\lambda)/L_a^2$, could be utilized, where $C'(\lambda)$ is a wavelength-dependent prefactor calculated by the following relation: $C'(\lambda) = C_0 + C_1/\lambda$, where $C_0 = -12.6$ nm and $C_1 = 0.033$. Surface chemical structure of the hard carbons was investigated through X-ray photoelectron spectroscopy using monochromatic Al K α radiation. Specific surface areas and porous properties of the hard carbons were analyzed by nitrogen adsorption and desorption isotherms at 77 K and carbon dioxide adsorption isotherms in the pressure range 0.019–794 mmHg (ASAP2020, Micromeritics, USA).

SAXS Analysis: The SAXS profiles were measured in the range of 0.02–0.7 Å⁻¹ with Cu K α radiation using NANOPIX (Rigaku) at the HANARO facility, Republic of Korea. Silver behenate powder was used as a standard sample for the data calibration of the q -space. All the acquired SAXS profiles were calibrated to volumetric scattering cross-section ($I^{cm^{-1}}$) through standard method with NIST (National Institute of Standards and Technology) glass carbon standard sample (SRM 3600, SN: A37), then converted to a specific scattering cross-section ($I^{cm^2g^{-1}}$) by normalization with effective bulk density ρ , which was determined by sample attenuation method.^[26] SASVIEW and Irena/NIKA package were used for model fitting of SAXS data.^[27]

Small-Angle Neutron Scattering (SANS) Analysis: The SANS measurement was conducted using the 40M SANS instrument at HANARO neutron facility, KAERI. The SANS dataset in the range of 0.03–0.9 Å⁻¹ was collected at sample-to-detector distance of 1.16 m with neutron wavelength of 5 Å. The absolute scaling to volumetric scattering cross-section ($I^{cm^{-1}}$) of the dataset was carried out by direct beam flux method using HANARO SANS data reduction software.

Model Fitting of SAXS and SANS Data for Porosity and Other Morphological Parameters of Micropores: Specific pore volume (unit: cm³ g⁻¹) and other morphological parameters of micropores including the pore–pore distance d , the correlation length ξ , the disorder parameter f_a , the average pore radius r , were calculated through model fitting of specific scattering cross-section by Teubner–Strey model.^[26] The final

microporosity, Φ_{pore} (unit: cm³/cm³) was calculated by multiplying the particle density to specific pore volume of each sample.

Electrochemical Characterization: Electrochemical tests for lithium-ion and sodium-ion storage behaviors of the hard carbon series samples were conducted with an automatic battery cycler (wbcs3000LE32_4, Wonatech, South Korea) and CR2032-type coin cells. Working electrode was prepared from a slurry method using the hard carbon active material, conductive agent (>99%, Alfa Aesar, USA), and poly(vinylidene fluoride) binder (M_w : 534 000, Sigma-Aldrich, USA) as a weight ratio of 8:1:1 in *N*-methyl-2-pyrrolidone (99.0%, Sigma-Aldrich, USA). The slurry was uniformly coated in Cu foil (99.8%, Welcos, South Korea) substrate, and dried in a convention oven at 120 °C for 1 h. The active material-loaded Cu foils were punched as a 1/2 in. diameter, where the active material loading densities were ≈ 2 mg cm⁻². The working electrode was assembled with a glass microfilter separator and a lithium or sodium metal foil as a reference/counter electrode. Electrolyte was prepared by dissolving 1 M LiPF₆ (battery grade, Sigma-Aldrich, USA) or 1 M NaPF₆ (98%, Sigma-Aldrich, USA) in ethylene carbonate (EC) and diethyl carbonate (DEC) mixture (1:1 v/v) solution, and 60 μ L of the electrolyte was used for each half-cell test. Galvanostatic discharge/charge tests were conducted at a current density of 20 mA g⁻¹, and EIS profiles were obtained at room temperature in the frequency range of 1 MHz to 50 Hz using an impedance analyzer (ZIVE SP1, WonAtech, South Korea).

Sequential Electrochemical Tests: The sodium-ion half-cells composed of the hard carbon working electrode, a sodium foil counter/reference electrode, and both polyethylene (PE, SB16C, Welcos, South Korea) and glass microfilter separators were assembled with the sodium-ion electrolyte (1 M NaPF₆ in EC/DEC). The sodium-ion half-cells were precycled through a galvanostatic discharge/charge process at a current density of 20 mA g⁻¹ over a voltage window of 0.01–2.7 V vs Na⁺/Na, and then galvanostatically sodiated by –0.01 V vs Na⁺/Na. The fully sodiated hard carbon working electrodes were extracted from the sodium half-cells and reassembled with a lithium foil counter/reference electrode, the new separator combination (PE + glass microfiber filter), and the lithium-ion electrolyte (1 M LiPF₆ in EC/DEC) under Ar atmosphere. The lithium-ion half-cells were galvanostatically lithiated by –0.01 V vs Li⁺/Li at a current density of 20 mA g⁻¹, and followed by being delithiated to 3.0 V vs Li⁺/Li. Then, the lithium-ion half-cells were galvanostatically cycled during 3 times over a voltage window of –0.01 to 3.0 V vs Li⁺/Li. The hard carbon electrodes were again extracted in the lithium-ion half-cells and reassembled with a sodium foil counter/reference electrode, the new separator combination (PE + glass microfiber filter), and the sodium-ion electrolyte (1 M NaPF₆ in EC/DEC) under Ar atmosphere. After sodiation by –0.01 V vs Na⁺/Na, the hard carbon electrodes were extracted from the sodium-ion half-cells, and reassembled as the lithium-ion half-cells by the same method to the previous step. The reassembled lithium-ion half-cells were galvanostatically cycled over the voltage window of –0.01 to 3 V vs Li⁺/Li during 3 cycles.

Computational Details: First-principle calculations based on density functional theory (DFT) were performed using generalized gradient approximation (GGA) with the Perdew–Berke–Ernzerhof functionals and the projector-augmented wave pseudopotentials as implemented in Vienna Ab initio Simulation Package.^[33] The hard carbon models were constructed based on a (4 × 4) supercell of 2 layers of hexagonal graphene with and without topological defects. A kinetic energy cutoff of 400 eV and gamma-centered k -point meshes of (4 × 4 × 4) for bulk and (4 × 4 × 1) for surface were applied. All structures were fully relaxed until the residual force in the supercell converges within 0.02 eV Å⁻¹. Since conventional GGA functionals described van der Waals interactions poorly, the D3-BJ correction method known to properly describe the physics of graphite and its lithium-ion intercalation was adopted.^[34,35] The surface- and bulk-chemisorption voltages of alkali metal ion (M) were calculated as follows

$$V_{\text{chemisorption}} = -\left(E(M^*) - E(^*) - E(M)\right) \quad (3)$$

where $E(M^*)$ and $E(^*)$ are DFT energies of hard carbon system with and without an alkali metal ion adsorption, and $E(M)$ is an atomic

energy of alkali metal calculated from bulk phase. Nudged elastic band calculations were performed to determine the diffusion barrier for alkali metal intercalants in hard carbon.

Preparation of Polymeric Hard Carbons: The polymeric hard carbon materials were prepared from different polymer precursors such as cellulose, lignin, silk protein, and polyester by two-step heat-treatment process. In the first heat-treatment process, the precursors were pyrolyzed in a tube furnace at 800 °C for 2 h under an Ar flow. Heating rate of 5 °C min⁻¹ and Ar flow rate of 200 mL min⁻¹ were applied for the process. The carbonaceous products were then thermally annealed in a graphite furnace at different heating temperatures of 1200, 1600, 2000, 2400, and 2800 °C for 2 h under Ar atmosphere. Different heating rates of 5 and 3 °C min⁻¹ were applied from 1200 to 2000 °C and from 2000 to 2800 °C, respectively.

Supporting Information

Supporting Information is available from the Wiley Online Library or from the author.

Acknowledgements

H.K. and J.C.H. contributed equally to this work. This research was supported by the Basic Science Research Program through the National Research Foundation of Korea (NRF) funded by the Ministry of Education (Grant Nos. NRF-2019R1A2C1084836 and NRF-2021R1A4A2001403) and the Ministry of Science and ICT (Grant No. NRF-2022R1C1C1011484). This work was supported by the KU-KIST School Program.

Conflict of Interest

The authors declare no conflict of interest.

Data Availability Statement

The data that support the findings of this study are available on request from the corresponding authors. The data are not publicly available due to privacy or ethical restrictions.

Keywords

alkali-ion storage mechanism, hard carbon anode, intercalation propensity, lithium-ion batteries, pore-filling mechanism, sodium-ion batteries

Received: October 4, 2022

Revised: December 8, 2022

Published online: February 12, 2023

[1] T. Enoki, M. Suzuki, M. Endo, *Graphite Intercalation Compounds and Applications*, Oxford University Press, Oxford, UK 2003.

[2] M. S. Whittingham, *Chem. Rev.* **2014**, *114*, 11414.

- [3] S. A. Freunberger, *Nat. Energy* **2017**, *2*, 17091.
- [4] A. Manthiram, *Nat. Commun.* **2020**, *11*, 1550.
- [5] A. Manthiram, *ACS Cent. Sci.* **2017**, *3*, 1063.
- [6] J. Lee, A. Urban, X. Li, G. Hautier, G. Ceder, *Science* **2014**, *343*, 519.
- [7] S. Choi, T.-W. Kwon, A. Coskun, J. W. Choi, *Science* **2017**, *357*, 279.
- [8] P. Pietsch, D. Westhoff, J. Feinauer, J. Eller, F. Marone, M. Stampanoni, V. Schmidt, V. Wood, *Nat. Commun.* **2016**, *7*, 12909.
- [9] G. M. Jenkins, K. Kawamura, *Nature* **1971**, *231*, 175.
- [10] J. R. Dahn, T. Zheng, Y. Liu, J. S. Xue, *Science* **1995**, *270*, 590.
- [11] E. Buiel, A. E. George, J. R. Dahn, *J. Electrochem. Soc.* **1998**, *145*, 2252.
- [12] Q. Meng, Y. Lu, F. Ding, Q. Zhang, L. Chen, Y.-S. Hu, *ACS Energy Lett.* **2019**, *4*, 2608.
- [13] Y. Morikawa, S.-I. Nishimura, R.-I. Hashimoto, M. Ohnuma, A. Yamada, *Adv. Energy Mater.* **2020**, *10*, 1903176.
- [14] B. Zhang, C. M. Ghimbeu, C. Laberty, C. Vix-Guterl, J.-M. Tarascon, *Adv. Energy Mater.* **2016**, *6*, 1501588.
- [15] S. Qiu, L. Xiao, M. L. Sushko, K. S. Han, Y. Shao, M. Yan, X. Liang, L. Mai, J. Feng, Y. Cao, X. Ai, H. Yang, J. Liu, *Adv. Energy Mater.* **2017**, *7*, 1700403.
- [16] J. M. Stratford, A. K. Kleppe, D. S. Keeble, P. A. Chater, S. S. Meysami, C. J. Wright, J. Barker, M.-M. Titirici, P. K. Allan, C. P. Grey, *J. Am. Chem. Soc.* **2021**, *143*, 14274.
- [17] Y. S. Yun, K.-Y. Park, B. Lee, S. Y. Cho, Y.-U. Park, S. J. Hong, B. H. Kim, H. Gwon, H. Kim, S. Lee, Y. W. Park, H.-J. Jin, K. Kang, *Adv. Mater.* **2015**, *27*, 6914.
- [18] P. Bai, Y. He, X. Zou, X. Zhao, P. Xiong, Y. Xu, *Adv. Energy Mater.* **2018**, *8*, 1703217.
- [19] Y. Qi, Y. Lu, F. Ding, Q. Zhang, H. Li, X. Huang, L. Chen, Y.-S. Hu, *Angew. Chem., Int. Ed.* **2019**, *58*, 4361.
- [20] S.-W. Zhang, W. Lv, C. Luo, C.-H. You, J. Zhang, Z.-Z. Pan, F.-Y. Kang, Q.-H. Yang, *Energy Storage Mater.* **2016**, *3*, 18.
- [21] H. Au, H. Alptekin, A. C. S. Jensen, E. Olsson, C. A. O'Keefe, T. Smith, M. Crespo-Ribadeneyra, T. F. Headen, C. P. Grey, Q. Cai, A. J. Drew, M.-M. Titirici, *Energy Environ. Sci.* **2020**, *13*, 3469.
- [22] G. M. Jenkins, K. Kawamura, *Polymeric Carbons: Carbon Fibre, Glass and Char*, Cambridge University Press, Cambridge, UK 1976.
- [23] A. Oberlin, *Carbon* **1984**, *22*, 521.
- [24] S. Y. Cho, Y. S. Yun, S. Lee, D. Jang, K.-Y. Park, J. K. Kim, B. H. Kim, K. Kang, D. L. Kaplan, H.-J. Jin, *Nat. Commun.* **2015**, *6*, 7145.
- [25] S. Y. Cho, Y. S. Yun, D. Jang, J. W. Jeon, B. H. Kim, S. Lee, H.-J. Jin, *Nat. Commun.* **2017**, *8*, 74.
- [26] D. Saurel, J. Segalini, M. Jauregui, A. Pendashteh, B. Daffos, P. Simon, M. Casas-Cabanas, *Energy Storage Mater.* **2019**, *21*, 162.
- [27] J. Ilavsky, P. R. Jemian, *J. Appl. Crystallogr.* **2009**, *42*, 347.
- [28] J. Park, S. Ha, J. Y. Jung, J.-H. Hyun, S.-H. Yu, H.-K. Lim, N. D. Kim, Y. S. Yun, *Adv. Sci.* **2022**, *9*, 2104145.
- [29] J. Um, S. U. Yoon, H. Kim, B. S. Youn, H.-J. Jin, H.-K. Lim, Y. S. Yun, *J. Energy Chem.* **2022**, *67*, 814.
- [30] Y. Wang, P. Puech, I. Gerber, A. Pénicaut, *J. Raman Spectrosc.* **2014**, *45*, 219.
- [31] M. Drüe, M. Seyring, M. Rettenmayr, *J. Power Sources* **2017**, *353*, 58.
- [32] H. Kim, J. C. Hyun, J. I. Jung, J. B. Lee, J. Choi, S. Y. Cho, H.-J. Jin, Y. S. Yun, *J. Mater. Chem. A* **2022**, *10*, 2055.
- [33] G. Kresse, J. Furthmüller, *Comput. Mater. Sci.* **1996**, *6*, 15.
- [34] C. R. C. Régo, L. N. Oliveira, P. Tereshchuk, J. L. F. Da Silva, *J. Phys.: Condens. Matter* **2015**, *27*, 415502.
- [35] O. Lenchuk, P. Adelhelm, D. Mollenhauer, *J. Comput. Chem.* **2019**, *40*, 2400.